

Clemson University

TigerPrints

All Theses


Theses

12-2022

Optical Control System for Atmospheric Turbulence Mitigation

Martyn Lemon
martynl@g.clemson.edu

Follow this and additional works at: https://tigerprints.clemson.edu/all_theses

 Part of the [Controls and Control Theory Commons](#), [Electromagnetics and Photonics Commons](#), and the [Systems and Communications Commons](#)

Recommended Citation

Lemon, Martyn, "Optical Control System for Atmospheric Turbulence Mitigation" (2022). *All Theses*. 3919.
https://tigerprints.clemson.edu/all_theses/3919

This Thesis is brought to you for free and open access by the Theses at TigerPrints. It has been accepted for inclusion in All Theses by an authorized administrator of TigerPrints. For more information, please contact kokeefe@clemson.edu.

OPTICAL CONTROL SYSTEM FOR ATMOSPHERIC TURBULENCE
MITIGATION

A Thesis
Presented to
the Graduate School of
Clemson University

In Partial Fulfillment
of the Requirements for the Degree
Master of Science
Electrical Engineering

by
Martyn Lemon
December 2022

Accepted by:
Eric Johnson, Committee Chair
Richard Groff
Suyi Li

ABSTRACT

Propagation of laser light is distorted in the presence of atmospheric turbulence. This poses an issue for sensing, free-space optical communications, and transmission of power. With an ever-increasing demand for high-speed data communications, particularly between satellites, unmanned vehicles, and other systems that benefit from a point-to-point link, this issue is critical for the field. A variety of methods have been proposed to circumvent this issue. Some major categories include the manipulation of the light's structure, an adaptive scheme at the optical receiver, scanning mirror systems, or a transmission of simultaneous signals with a goal to improve robustness.

There is an inherent advantage to a turbulence mitigation scheme that can be performed on the transmission side of an optical link. By rapidly probing a turbulent volume by varying a beam's spatial and phase characteristics, the best transmission mode for an optical beam can be determined and controlled in real time. With the fast mode-switching capabilities of the HOBbit (Higher-Order Bessel-Beams Integrated in Time) system, the dynamics of turbulence can be probed incredibly quickly. This work presents an optical control system that takes advantage of such a probing method, and greatly improves power efficiency and successful recovery of data through environments with strong turbulence.

DEDICATION

This work is dedicated to my family and friends who have supported me through my studies. I could not have done it without your love and encouragement.

ACKNOWLEDGMENTS

I would like to sincerely thank my advisor Dr. Eric Johnson. His mentorship has helped me develop into a better engineer and pushed me to always do my best work. I am grateful for the opportunity he gave me as an undergraduate, which opened the door to my interest in graduate school. Additionally, I am grateful for his patience, enthusiasm, and leadership in our laboratory. He has been a wonderful role model.

I would like to thank my committee members, Dr. Richard Groff and Dr. Suyi Li, for their valuable time and advice. Their wisdom in engineering and mathematics supported the creation of this project.

I want to thank Dr. Keith Miller for his supervision and assistance in the lab and with many experiments, and his great intuition for problem solving. I thank Evan Robertson, Justin Free, Kunjian Dai, and everyone else in our lab who have helped me on my journey of completing this thesis. Their support and collaboration for this project are just as important and meaningful as any work of my own. Their friendship made the laboratory a great place to be.

Lastly, I would like to thank my family and close friends. Thank you for dispelling my self-doubt and always believing in me.

Funding for this research was provided by the following grants: ONR MURI N00014-20-1-2558 and ONR (N00014-16-1-3090, N00014-17-1-2779, N00014-20-1-2037).

TABLE OF CONTENTS

	Page
TITLE PAGE	i
ABSTRACT.....	ii
DEDICATION.....	iii
ACKNOWLEDGMENTS	iv
LIST OF TABLES.....	vii
LIST OF FIGURES	viii
CHAPTER	
I. INTRODUCTION	1
The Need for Turbulence Mitigation.....	1
Review of Existing Methods.....	2
II. MOTIVATION TO PROBE WITH HOBBIT	4
III. CONTROL METHODOLOGY.....	9
Probing and Experimental Setup	9
Controller and Algorithm.....	12
Hardware Connectivity and Python Advantages and Disadvantages	16
IV. PERFORMANCE ASSESSMENT	19
Introduction.....	19
Power Efficiency.....	19
Data Recovery.....	23
Multiple Channels and Higher Data Rate	26
V. CONCLUSIONS AND FUTURE WORK.....	30

Table of Contents (Continued)	Page
APPENDICES	33
A: Control Algorithm Code	34
B: Circuit Diagrams	42
C: Description of Data Signals	44
D: Optical Transform of HOBBIT System	46
E: List of Publications	49
REFERENCES	50

LIST OF TABLES

Table		Page
2.1	Turbulence Strengths	5

LIST OF FIGURES

Figure		Page
2.1	Left to Right: OAM Charge 5, 10, and 15. Black circle represents Gaussian spot.....	5
2.2	Maximal Beam Wander Correction.....	7
2.3	Guided Modes in Turbulence.....	8
3.1	(a) Rendering of modified HOBBIT with beam profiles. (b) Picture of HOBBIT system used in experiment.....	9
3.2	(a) Diagram of optical path through VTG. (b) Picture down length of VTG.....	11
3.3	(a) Receiver setup rendering. (b) Receiver setup picture.....	12
3.4	Experimental Setup.....	12
3.5	Control System Diagram.....	15
3.6	(a) Ambient turbulence conditions, camera image of scan (left), camera of decision (middle), spectrogram of probing results (right). (b) Strong turbulence ($r_0 = 3.8$ mm), same pattern. Red circle illustrates strong beam state.....	15
4.1	Received optical power in strong turbulence with (a) control system off and (b) control system on.....	20
4.2	Disparity in realizations above power threshold at different turbulence strengths.....	21
4.3	(a) mean BER for turbulence strength, control on. (b) percent BER below FEC limit.....	24
4.4	(a,c) realization above FEC limit. (b,d) realization below FEC.....	25
4.5	(a,c) beam deflected off axis. (b,d) beam guided to receiver.....	25

List of Figures (Continued)

Figure		Page
4.6	(a-f) consecutive realizations. (g) transmission channels. circled. (h,i) locked beams	27
4.7	Multiple channels with higher OAM range	28
4.8	32 QAM Constellation.....	29

CHAPTER ONE

INTRODUCTION

The Need for Turbulence Mitigation

In the atmosphere, turbulence is a common phenomenon where temperature within the air is inhomogeneous throughout space. These temperature fluctuations create a variation in the refractive indices of the medium, which distort and deflect any waves propagating through [1]. A turbulent volume of air can be represented by a superposition of random phase screens [2-4], which can each deflect the incoming wave to a slightly different angle. For an optical wave, particularly a laser beam, this net result produces a well characterized effect of beam wander [5-7] that can deflect a beam from its desired target. This is particularly undesirable for laser applications such as communications, especially between ground stations and satellites [8], remote sensing such as LIDAR [9], and directed energy [10], which are all rapidly developing and increasingly important fields. Due to the temporal variance of turbulence, there are instants where light may travel through the turbulence seemingly undisturbed, depending on the input mode of light [11]. Depending on the spatial distribution of the light intensity and the phase tilt of the beam as it enters the turbulent air, the random phase screens that compose the transfer function of the atmospheric turbulence can have a waveguiding effect to a desired location [2,3,11]. With advances in optics, electronics and computing, many methods have been proposed and demonstrated to successfully mitigate the fluctuations in a received beam due to turbulence [12-22]. The presented solution offers a new way to

exploit the random waveguiding effect, and greatly improve the average power delivery to a target and support the stability of a communication link.

Review of Existing Methods

A variety of methods have successfully reduced the effect of turbulence on optical applications. [12] describes a method to improve astronomical imaging using an algorithmic approach, which could greatly reduce the blurring resulting from the image wander, similar to the beam wander which is further described in Chapter 2. [13] showed a highly effective method to improve resiliency of a communication link by expanding the modes collected by an aperture and bolstering the signal fidelity using pilot tones. [14] and [15] each demonstrate methods to expand the capabilities of an optical receiver, using a maximum-likelihood sequence estimator and expansion of receiving fibers, respectively. These methods all become limited by the size of the aperture, as the beam wander effects of turbulence and spatial incoherence increase with turbulence strength and propagation distance.

Several other methods use a deformable or fast steering mirror system with a wavefront sensor of sorts as feedback [16-19]. [17] showed a 1.5kHz refresh rate deformable mirror with 45 separate actuators, using a Shack-Hartmann sensor as feedback, while [19] saw an adaptive-optic system with up to then tens of kHz. Ultimately, these methods are limited by the mechanical switching speeds of the mirrors, and the mechanical complexity of deformable mirrors along with the associated electronic controls. [20] investigated the use of orbital angular momentum (OAM) modes for improving resiliency, which is a relevant detail to the proposed system method, which

exploits this light structure. [21] describes a variety of light structure modes, and how different modes tend to deflect and distort different through a given portion of atmospheric turbulence. There have been many studies published pertaining to structure light through turbulence, which are reviewed thoroughly in [21]. [22] is a good review article covering several ways that turbulence is mitigated for optics applications. Unlike many of the mitigation schemes described, the presented system is not limited by aperture size in increasing turbulence and has switching rates that can far exceed conventional mirror systems thanks to its fully electronic actuation, described further in Chapter 2.

CHAPTER TWO

MOTIVATION TO PROBE WITH HOBBIT

The HOBBIT system, originally demonstrated in [23], allows for rapid switching of a vortex beam's orbital angular momentum (OAM) via its topological charge number. This charge number represents the number of 2π rotations of a beam's phase in a propagation length equal to the wavelength [24]. The switching speed of the HOBBIT system in [23] was shown to be up to 400kHz, with the note that this could be pushed even further into the MHz range depending on the beam diameter and type of acousto-optic deflector (AOD) used. By altering the configuration of optical elements in the HOBBIT system, described in detail in Chapter 3 and Appendix D, this architecture can be used to manipulate the location and phase gradient of a single Gaussian beam about a ring footprint, incurred by the log-polar coordinate transform of the HOBBIT system. Rather than spreading a Gaussian beam into an elliptic shape before wrapping via the log-polar optics [23], a single Gaussian spot could be deflected, effectively moving it around in space. With the phase gradient incurred by another AOD, this beam can be directed with a tilt, similar to a conventional motorized mirror.

Using the modified HOBBIT system, described further in Chapter 3, an arbitrary phase profile can be applied to the input beam, resulting in the tilt correction necessary for turbulence mitigation. Depending on an applied electronic frequency, an arbitrary OAM charge number can be applied to the circular probing footprint, which results in a phase gradient across the Gaussian beam that is tangent to the circle. Figure 2.1 illustrates the concept:

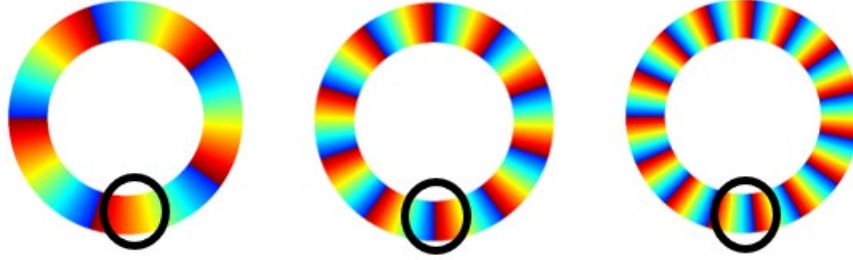


Fig. 2.1. Left to Right: OAM Charge 5, 10, and 15. Black circle represents Gaussian spot

With an OAM charge of 5, there is a relatively small phase gradient across the black circled region, representing the phase across the Gaussian beam. While this spot is not to scale, it illustrates how the beam is tilted, and that this phase gradient will always be tangential to the ring. The fact that this phase tilt is tangential to the circle is a key motivation for using the HOBBIT system for turbulence mitigation. Depending on where the Gaussian beam is shifted around this circle, the direction of its skew angle will be different. Skew angle in the context of OAM refers to the deflection of the Poynting vector with respect to the propagation of a beam with a helical phase [25]. For this singular Gaussian spot in the helical phase map, the OAM charge number will dictate how far the beam is deflected, depending on the radius of the ring. Additionally, since the phase creating the deflection is tangential to the ring, the rotation angle will determine which direction the beam will be deflected.

In atmospheric turbulence, it is well known that thermal inhomogeneity within a volume of air or another medium create a unique refractive index, which can deflect a beam off-axis from its detector [1-4]. To quantify how much the beam can be diffracted, several metrics to quantify the strength of turbulence exist. Two that will be considered in this document are the Fried parameter r_0 and the refractive index structure constant C_n^2

[2,3]. Several values of these parameters are created experimentally, which will be used as an independent variable in several of the experiments of Chapter 4. There, they are referred to by r_0 , but Table 1 will compare the two metrics, for a propagation distance of 60m used in all experiments:

Table 2.1. Turbulence Strengths

r_0 (mm)	700	49.9	16.4	8.6	6.7	5.4	4.5	3.8
C_n^2 (m ^{-2/3})	1.0e-15	4.2e-14	2.7e-13	7.9e-13	1.2e-12	1.7e-12	2.3e-12	3.1e-12

Using a Gaussian beam with diameter close to the size of r_0 , there is a succinct expression for the variance of the beam due to turbulence [2-4]:

$$\langle \beta^2 \rangle \approx 0.54 Z^2 \left(\frac{\lambda}{2w_0} \right)^2 \left(\frac{2w_0}{r_0} \right)^{\frac{5}{3}} \quad (1)$$

Equation 1 can be used to describe the radial deflection range of one standard deviation for a Gaussian beam given the parameters. Using the maximal turbulence strength of the experiment $r_0 = 3.8\text{mm}$, a propagation length $Z = 60\text{m}$, optical wavelength $\lambda = 532\text{nm}$, and Gaussian beam radius $w_0 = 4.2\text{mm}$, the variance is calculated to be about $29.2\mu\text{m}$ of deflection off-axis. To account for up to 99% of possible deflection distances, three standard deviations are used to generate a maximal deflection range of up to $\sim 90\mu\text{m}$. For the modified HOBBIT system to be able to correct for this maximal deflection, the range of OAM values should be determined according to the maximal skew angle that the system can apply:

$$\theta = \frac{l}{kr} \quad (2)$$

Equation 2 from [25] is used to find this angle θ , which can be equated to $90\mu\text{rad}$ using the small-angle approximation. Using the wave number k for the 532nm light and a

ring radius $r = 17.5\text{mm}$ (see Chapter 3), the required OAM charge number l to correct for this deflection is found to be about 18. The direction of this correction is related to the direction of the phase gradient, which is controlled by the position of the beam around the ring footprint. With the log-polar transform, the HOBBIT system architecture provides a convenient, one-dimensional basis for correcting any direction of beam wander.

Due to hardware limitations, further discussed in Chapter 3, the maximum OAM range implemented on the system was ± 15 . Using Equation 2, this means the maximal correction is about $73\mu\text{m}$. This falls within 2 standard deviations of the beam wander variance, so it is expected that at $r_0 = 3.8\text{mm}$, about 90% of realizations can be fully corrected to the initial axis of transmission. Figure 2.2 shows the issue that can occur if insufficiently high OAM range is used:

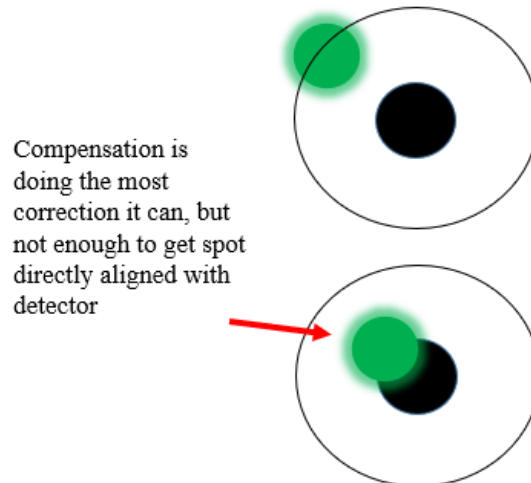


Fig. 2.2. Maximal Beam Wander Correction

The top graphic in Figure 2.2 shows an instance in time where the turbulence has deflected the beam significantly off-axis, to the limit of where it may travel at that strength. The lower graphic shows what happens if the highest possible OAM is applied

to the input beam, but the phase gradient is not steep enough to completely restore the initial position. It is expected that more power would be recoverable than if no compensation were applied, but it may not be enough to meet a recoverability threshold. Figure 2.3 illustrates the concept of finding guided modes through turbulence:

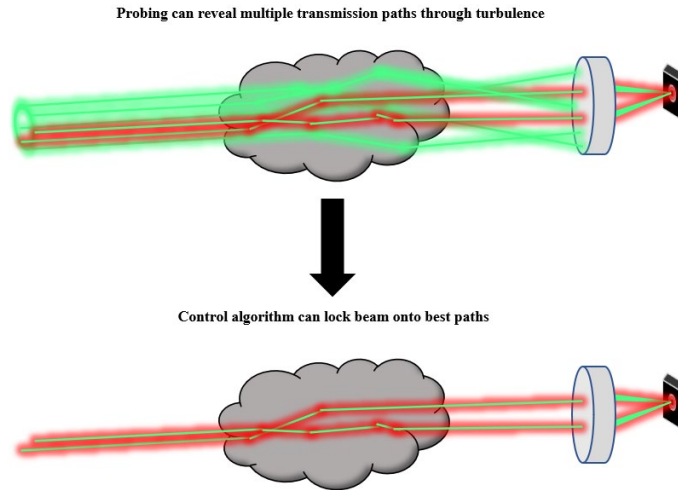


Fig. 2.3. Guided Modes in Turbulence

The modified HOBbit system has extremely fast switching speeds for different beam modes and has been shown to have enough compensation ability to effectively compensate for atmospheric turbulence a majority of the time. With this motivation, the system was built, and a control algorithm was developed to test the hypothesis.

CHAPTER THREE

CONTROL METHODOLOGY

Probing and Experimental Setup

To rapidly manipulate the spatial location and phase gradient of the Gaussian beam, a modified HOBBIT system [23,26-28] was used. This HOBBIT system was configured differently than discussed in [23], because both the spatial and phase dimensions needed electronic control. The standard HOBBIT system controls the OAM charge number of an asymmetric perfect vortex beam, but this configuration used two acousto-optic deflectors (AODs). The first AOD controlled the azimuthal location or rotation angle of the Gaussian beam about a vortex footprint, created by the log-polar optics at the end of the HOBBIT optical path (see Appendix D for a detailed description of this modified HOBBIT's overall optical transform). The second AOD controls the phase tilt of the Gaussian beam, which can be quantified by an OAM charge number. Figure 3.1 shows the layout of the new HOBBIT system:

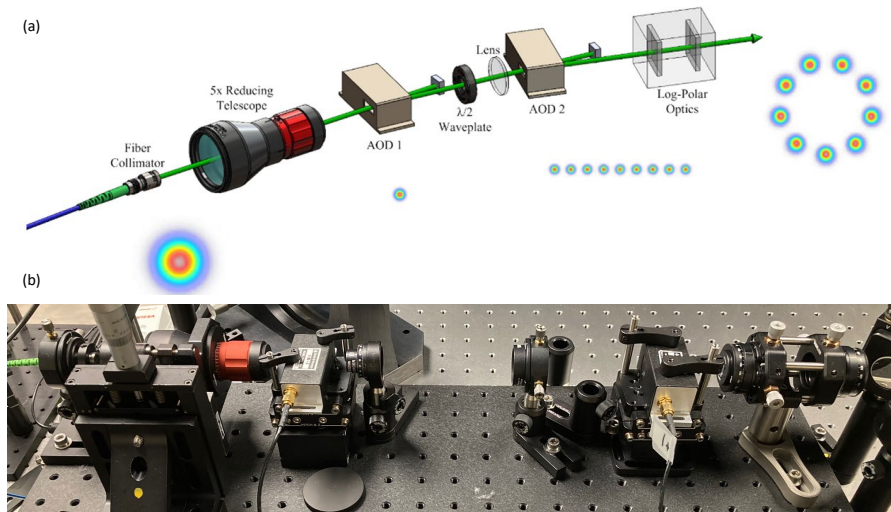


Fig. 3.1. (a) Rendering of modified HOBBIT with beam profiles. (b) Picture of HOBBIT system used in experiment

In Fig. 3.1 (a), the overlaid beam profiles show a discretization of the probing sequence. A singular Gaussian beam is coupled into the first AOD, which deflects the beam to a different spatial location on a line. The second AOD applies the phase shift, and the spot is wrapped onto the circular footprint by the log-polar optics. Finalizing the derivations in Appendix D, the equation expressing the electric field immediately exiting the HOBBIT system is given by:

$$E(r, \theta) = \exp\left(-\frac{(r - \rho_0)^2}{\rho_0^2 w^2} - \frac{(\theta - \theta_0)^2}{w^2} - j(m\theta + 2\pi(f_c + f_{A1} + f_{A2})t)\right) \quad (3)$$

Where $\rho_0 = 1.75\text{mm}$ is the radius of the probing footprint, $w = \sigma / A = 0.24$, $\theta_0 = \Delta f_j \lambda F / (AV)$ is the rotation angle about the footprint, which depends on the applied electronic frequency to the first AOD, and $m = 2\pi A \Delta f_2 / V$ is the topological charge number of the field which depends on the applied electronic frequency to the second AOD. The approximation $\ln(r / \rho_0) \approx r / \rho_0 - 1$ for $0 \leq r / \rho_0 < 2$ was used to derive Eq. (3). This equation approximately describes a Gaussian beam of width $\rho_0 w$ shifted by the probing radius, with tunable rotation angle θ_0 and tunable OAM charge number m . Before propagation through atmospheric turbulence, the beam is expanded by a 10x telescope resulting in a Gaussian beam with a diameter of 8.4mm, shifted by the new probing radius of 17.5mm. The near-field of this output beam is propagated through the turbulence, resulting in a Gaussian profile all the way to the receiver.

To simulate atmospheric turbulence, a similar setup of the variable turbulence generator (VTG) tunnel in [29] was used. This tunnel most closely follows the Kolmogorov spectrum of turbulence [30]. The beam is deflected using 4 mirrors to pass

through the tunnel 3 times, resulting in a total propagation length of 60m. Figure 3.2 shows the setup:

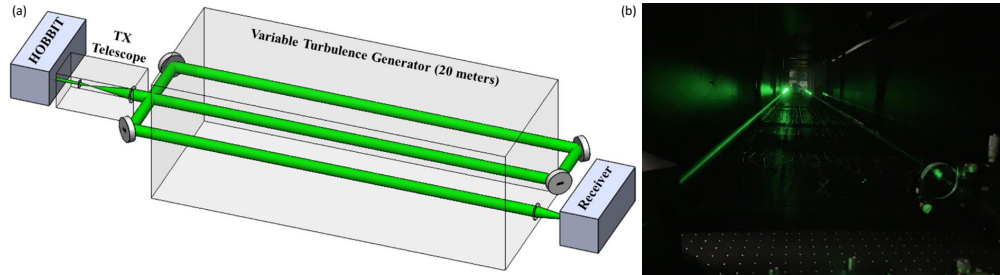


Fig. 3.2. (a) Diagram of optical path through VTG. (b) Picture down length of VTG.

By controlling the electrical power to the heating elements of the VTG, different strengths of atmospheric turbulence can be generated, following Table 1 in Chapter 2.

A receiver setup was designed which provided feedback to the controller and measured optical power and transmitted data signals. After the 60m propagation length, the beam is passed through a 500mm lens to perform a Fourier transform. 80% of the collected beam is diverted toward a multi-mode fiber with diameter of $50\mu\text{m}$ using a beam splitter. This fiber is connected to a photoreceiver (RXM10BF) with a bandwidth of 10GHz to receive data signals. To measure the optical power, the fiber was connected instead to a DET10A detector with responsivity of 250mA/W at the optical wavelength of 532nm. That detector was amplified by 15dB using the amplifier circuit described in Appendix B. Both detectors were sampled by an oscilloscope (MSO71254C). A small portion of the beam is directed towards an avalanche photodiode detector (APD120A2) with a bandwidth of 50MHz, which was used for probing feedback to the controller. This detector is wired under the VTG to the controller. Lastly, a small portion of this branch is diverted using another beam splitter to a high-speed camera (Phantom T-1340), used to

capture the control process. The camera operates at 1000 frames per second with an integration time of $45\mu\text{s}$. A rendering and visualization of the receiver setup is shown in

Figure 3.3:

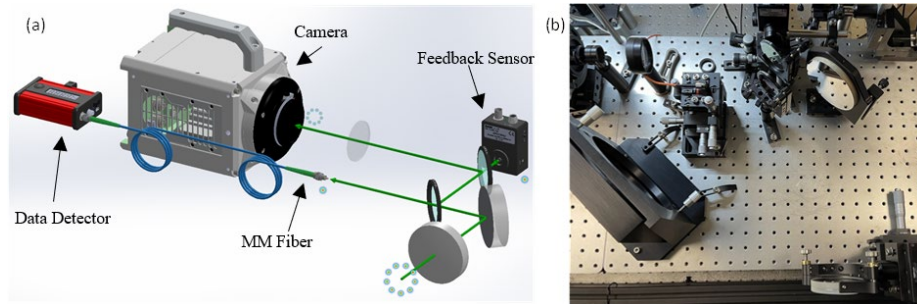


Fig.3.3. (a) Receiver setup rendering. (b) Receiver setup picture

A diagram of the entire experimental setup is shown in Figure 3.4:

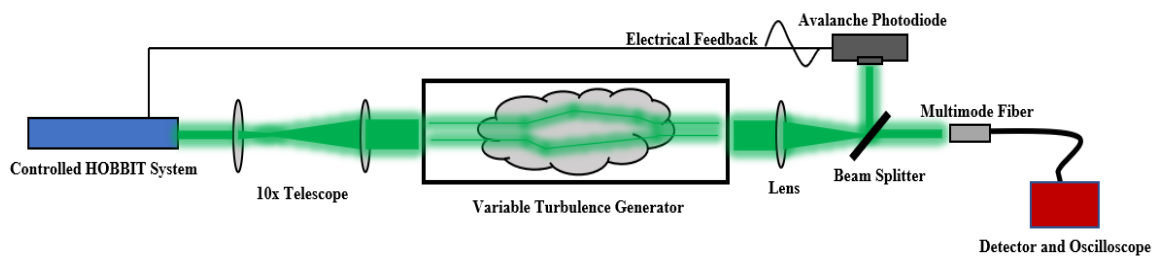


Fig. 3.4. Experimental Setup

Controller and Algorithm

To control the HOBBIT system, the electronic waveforms applied to the AODs need to be changed rapidly. To make the most effective system, the control process needs to be as fast as possible, and properly synchronized with the probing sequence. The ideal controller for this system would require an analog-to-digital converter capable of sampling at a rate of at least 12.5MHz to properly measure the feedback of the probing sequence. The controller would also need a processor capable of determining which combination of OAM and rotation angle during the sequence corresponds to the maximal

feedback voltage, to determine which combination should be used to lock the beam to transmit data and/or power. Lastly, the controller would need a fast digital-to-analog converter to generate the correct waveforms for the two AODs to lock the beam at the best OAM and rotation angle combination.

To implement this controller, a hybrid between two products was developed. Due to availability of equipment in the lab, constraints on available products, and desired timeline for the project, the waveform generation was performed entirely on an arbitrary waveform generator (Tektronix AWG5208). This device offers the capability to create waveform sequences, which can be used to play specific frequencies indefinitely, but switch to a different frequency when a specific control signal is applied to a connector on the device.

To sample the feedback from the probing sequence, determine the best beam location, and apply the proper control signal to the AWG, a proprietary instrumentation board, the *ScopeFun*, was used. This board had several attractive features: It was relatively inexpensive and had a 250MHz analog-to-digital converter, a fast FPGA, and enough digital I/O pins to control the AWG. The critical feature of the *ScopeFun* was its Python API. While custom firmware could be developed for *ScopeFun* to implement the control algorithm, the Python API allowed for rapid development and prototyping in Python on a PC, which communicated with *ScopeFun* via USB to control its hardware. The full Python script used to implement this project is shown in Appendix A.

Due to the limitations of the AWG, the probing sequence was limited to 256 waveforms. The control signal, which allows the AWG to switch between a probing

waveform and the discrete waveforms for each position within that sequence, was only 8 bits. Within this constraint, the probing resolution was limited to 7 values of OAM, and 35 rotation angles around the ring. The probing sequence begins by stepping the Gaussian beam around the circular path, from an angle of $-\pi$ to π . After one complete revolution, the OAM charge number, realized by the second AOD, was incremented, changing the phase profile of the probing path (see Figure 1 in Chapter 2). Then, the incrementation through rotation angles begins again, repeating in this fashion until all OAM values have been probed. With the maximal resolution constraint, the OAM charge values chosen were from -15 to 15, with a step of 5. Each of the total of 245 beam states was held for 615ns during the probing sequence, giving a total time to probe with this resolution of $\sim 151\mu\text{s}$. This shows that the configuration of the HOBBIT speed can switch modes at a rate of over 1.6MHz. This probing speed is fundamentally limited by the acoustic velocity of the AODs: for a new beam state to occur, the new acoustic frequency generated in the AOD crystal must fully propagate across the width of the beam before the new beam state output is realized.

The *ScopeFun* samples an entire probing sequence worth of voltage from the feedback detector to use in its decision-making process. The algorithm computes the mean feedback voltage of each beam state across all samples and determines the maximum value and its index within the array of voltages. Since the sequence through each of the beam states in the probing space occurs in a known order, the algorithm can use this order to decide which combination of OAM and rotation angle coupled the highest amount of power to the detector. The *ScopeFun* then commands the AWG to lock

the beam in that state using the digital I/O ports and uses a pin to trigger the transmission of the communication channel if desired. Then, the algorithm delays execution for a specified duration to maintain the beam's coupling through the instantaneous turbulence state, and then resets the AWG to the probing sequence to repeat the process again. A block diagram of the control algorithm is shown in Figure 3.5:

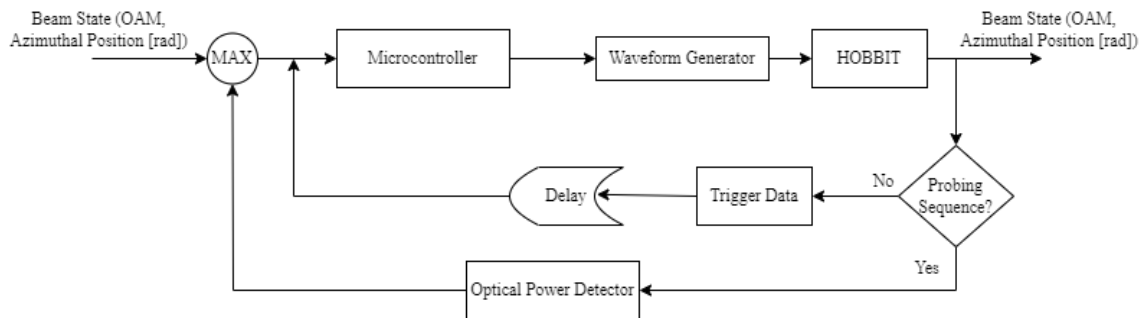


Fig. 3.5. Control System Diagram

A visualization of the probing and decision-making process is shown in Figure 3.6:

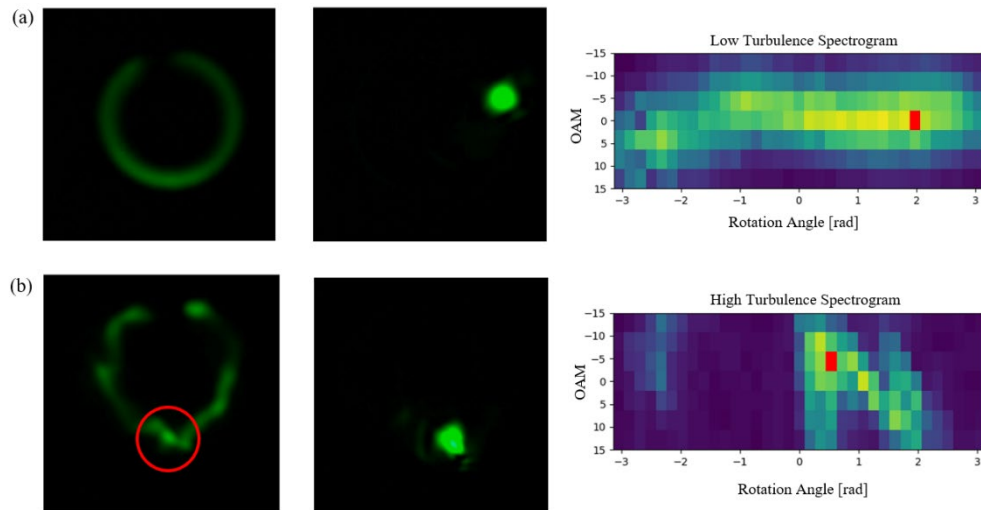


Fig. 3.6. (a) Ambient turbulence conditions, camera image of scan (left), camera of decision (middle), spectrogram of probing results (right). (b) Strong turbulence ($r_0 = 3.8\text{mm}$), same pattern. Red circle illustrates strong beam state.

Figure 3.6 shows some high-speed camera images of the scanning and decision-making process captured during the experiments described further in Chapter 4. The left column shows complete probing rings, which appear continuous due to the camera's integration time. These rings are not continuous but represent where the beam is moved in the rotation angle dimension of the probing space. The phase tilt induced by OAM is not seen, but the spectrograms in the right column show the relative optical power transmitted through the turbulence, with OAM on the y-axis and rotation angle on the x-axis. The central column shows a fixed beam, held constant once the best beam state is determined.

Hardware Connectivity and Python Advantages and Disadvantages

Hardware Connectivity

When the probing sequence begins, the AWG sends a pulse to the *ScopeFun* microcontroller to begin sampling the feedback detector. This pulse is calibrated for a specific delay, which corresponds to the electrical length between the feedback detector and the other side of the tunnel, where the controlled HOBbit system is. As soon as the pulse arrives to the microcontroller, the first voltage output from the detector can be sampled by the *ScopeFun*'s ADC channel 1. The board has now captured a digital waveform, which is stored into a USB data packet and sent to the PC attached to the *ScopeFun*. After the algorithm determines the best beam state and the proper 8-bit signal command, the digital I/O pins are used to switch the signals on the AWG's pattern-jump connector using IRFZ44N MOSFETs. The circuit showing these connections is shown in Appendix B. The MOSFETs were necessary to drive the pattern-jump pins low because

they were normally set to 5V above the AWGs reference ground, and the *ScopeFun* could only drive the voltage down a maximum of 3.3V to its logical ground with the I/O pins alone. It was experimentally determined that driving the pattern jump pins to 1.7V was insufficient to switch the logical state of the AWG pattern jump, so instead the MOSFETs switched the pattern jump pins to a short with the AWG reference ground, driving them down to 0V and switching the logic. For this reason, all the digital I/O logic in the algorithm is inverted to account for this circuit connection.

Python Advantages and Disadvantages

The main advantage to using the Python API to control the *ScopeFun* is its ease of development. The included functions handle all the hardware access, and it is intuitive to use, with a very shallow learning curve. Additionally, using Python allows integration and usage of other Python libraries, which can improve visualization and code flexibility. In the script, shown in Appendix A, several additional libraries are used, with the most prominent and important being NumPy. The NumPy library is a widely supported package for Python that allows for fast computation of matrix algebra, similar to MATLAB. NumPy is written in C, and as such has a very fast runtime. Runtime on a PC is incredibly fast—the computation for the best beam state is in the range of 100 μ s. Python also allows for easy customization of the control code for different experiments and gives room to grow for more complex control schemes on future systems. Additionally, using a PC as the user interface for the system makes it much easier to debug, tune, and use for a wide range of experiments.

The main advantage to the Python API is also its biggest disadvantage: the connection to a PC. Since the *ScopeFun* must transfer all the sampling data over USB to the PC running the Python script, and the PC must send the commands back over USB to reconfigure the hardware on the *ScopeFun*, there is delay introduced. It was experimentally measured that every command to reconfigure the hardware on the microcontroller took $\sim 100\mu\text{s}$, and several of these commands were required to successfully implement the control algorithm. This brought the total execution time of each cycle of the algorithm to anywhere between $\sim 750\mu\text{s}$ to 1ms, which while fast, could be reduced if the algorithm could run entirely on the *ScopeFun*'s FPGA. While this delay is the main drawback of the control implementation, it is possible that future iterations of this turbulence mitigation scheme could use a fully embedded algorithm, and immediately remove these extra delay steps. It is also worth to note that the *ScopeFun* board has two AWG channels of its own, but these were not used since they suffered from a much greater delay (up to 8ms) to reconfigure using the API. Perhaps an embedded version of the algorithm could leverage the built-in AWG channels and remove the need for the dedicated AWG box.

CHAPTER FOUR

PERFORMANCE ASSESSMENT

Introduction

This chapter is divided into three sections to reflect the three main criteria used to assess the efficacy of the HOBBIT turbulence mitigation system. The first is power efficiency—measuring how much optical power is preserved at the receiving aperture in strong turbulence compared to ambient conditions is of utmost importance. If the received power at the detector is less, this directly reduces the signal to noise ratio of data modulated on the beam, worsening its recoverability. Due to limitations of the oscilloscope, it was necessary to measure received optical power and data separately. The detector used for measuring the power was different than the one used for data, so separate experiments were conducted for both power and data, keeping as many variables constant as possible.

After examining the power loss in turbulence with the controlled system on vs. off, the recoverability of the 5 Gbit/s PAM2 signal (see Appendix C) will be presented. This will quantitatively evaluate the performance gain of the system through turbulence vs. a non-mitigated laser beam with the same modulated data. Lastly, some qualitative assessments will be made about the probing information, and a summary of a qualitative test performed with a higher data rate signal: a 25 Gbit/s 32QAM (see Appendix C).

Power Efficiency

To determine the optical power loss through turbulence, the first step was to find out the received optical power in ambient conditions. Using an average power level of

10.5mW into the HOBBIT system, about 2mW on average entered the VTG tunnel. After the receiving optics, an average power of 675 μ W was received into the multimode fiber that connects to the oscilloscope. This 675 μ W was used as the reference level to compare the loss due to turbulence for transmissions with the control system versus without. To measure the power, 1244 realizations were captured on the oscilloscope. Each realization was 3ms long, to mimic the paradigm necessary for the data experiment. Figure 4.1 shows the received power over the 1244 realizations in the maximal turbulence strength, a Fried parameter $r_0 = 3.8$ mm:

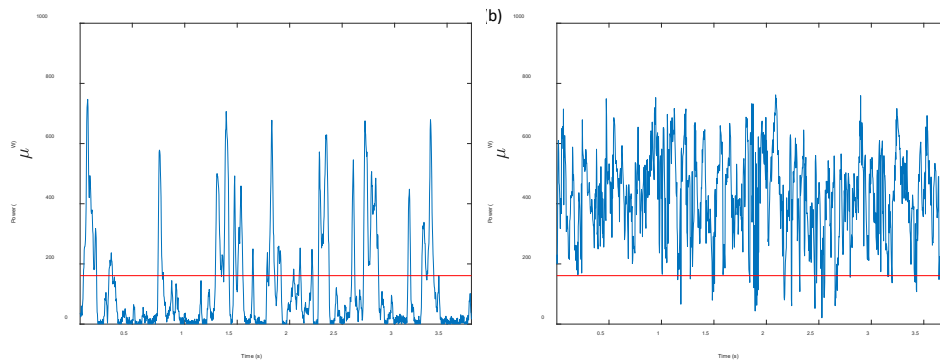


Fig. 4.1. Received optical power in strong turbulence with (a) control system off and (b) control system on

In Fig. 4.1 (a), the recovered optical power for a fixed Gaussian beam is shown. The fluctuations due to turbulence can clearly be seen. There are several spikes where the received power reaches the level at ambient conditions, but the average power is only 118 μ W. By contrast, Fig. 4.1 (b) shows the received power with the control system on. The average received power for this test was 425 μ W. The red line on each graph indicates the fade threshold for the signal. This was chosen to be 6dB below the reference power, at a level of 160 μ W. This threshold corresponds closely to the forward error correction (FEC) limit for the PAM2 signal used in the data recovery section (see Fig. 1

in Appendix C). The standard deviation in power for the controlled experiment was $146\mu\text{W}$, significantly higher than that in the ambient experiment which was $38\mu\text{W}$. This deviation is likely due to the variance in strength of transmission channels in turbulence. Sometimes, even the best transmission path within the probing volume is less than ideal, and only a portion of the total input power is delivered to the receiver.

One useful insight to glean from these results is the average persistence of a good transmission channel over a given setpoint for the turbulence conditions of the experiment. Assessing the peaks above the threshold limit for Fig. 4.1 (a), the average duration is about 40ms. This means that generally, a good transmission channel will exist in a given spatial location for roughly this window before moving past the beam, and the beam should be moved to a new location in the probing space. Figure 4.2 illustrates the differences between the control system and the non-controlled system at different levels of turbulence:

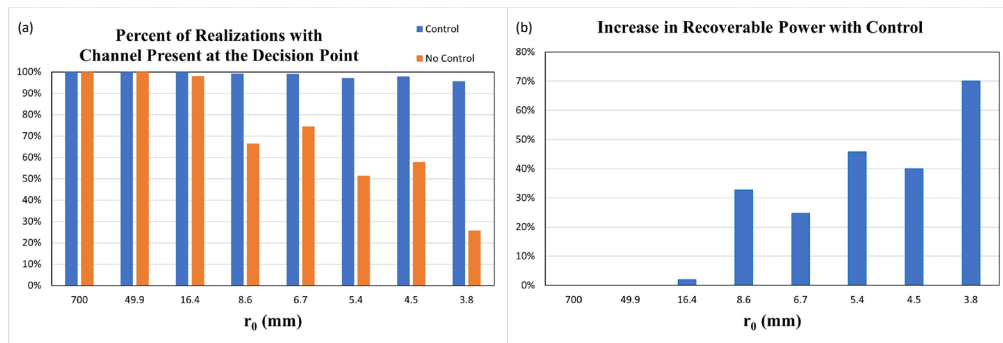


Fig. 4.2 Disparity in realizations above power threshold at different turbulence strengths.

The percentage of 1244 realizations at each of 8 different turbulence conditions above the 6dB fade threshold are compared. It is easily seen in Fig. 4.2 (a) that as turbulence increases, there is a greater gap between the control system and baseline. Fig. 4.2 (b)

shows the percent difference between the two datasets, showing a clear improvement in recoverable power with the control system. One distinct difference between the controlled system and the uncontrolled system is the nature of the realizations below the threshold. During the controlled experiment, every realization below the 6dB fade threshold was still above the noise floor of the oscilloscope. By contrast, many of the realizations of the uncontrolled system are completely lost and well below the noise floor.

In the strongest turbulence strength, $r_0 = 3.8\text{mm}$, about 90% of realizations were above the cutoff threshold. As discussed in Chapter 2, the controlled HOBBIT system can correct for a specific range of beam wander due to a given turbulence level. Depending on the applied OAM, the skew angle will tilt the Gaussian beam to give a shift of a given length, according to equation 2 in Chapter 2. For the experiment, a range of -15 to +15 OAM was used to probe and correct the beam, which results in a maximal correction of $73\mu\text{m}$. Recall the derivation in Chapter 2 of the maximal beam wander over 60m of propagation in the turbulence conditions described, of up to $90\mu\text{m}$. Since the system could not correct up this maximal range, it is expected that some realizations would be below the correction threshold. If the gaussian beam was deflected by $90\mu\text{m}$ from the receiving aperture and corrected by $73\mu\text{m}$, then only a small fraction of the total power will be coupled into the receiver. Figure 2.2 expressed this concept. It is clear that a future version of this turbulence mitigation scheme would benefit from an increased range in OAM.

Data Recovery

The next important evaluation of the system is the performance of a communication link. Using the PAM2 modulation scheme, a 5Gbit/s data signal was modulated onto the beam. See Appendix C for a thorough description of the data signal used in this experiment. To measure the performance of the communication link, the primary metric used is the bit error rate (BER). This quantity represents the percentage of bits in a transmission that are incorrect. When the signal-to-noise ratio (SNR) of the data signal is too low, the noise level can sufficiently sway one of the two voltage levels used to demodulate the PAM2 scheme, causing a bit error. When the beam is perturbed by turbulence and deflected off-axis, this SNR will decrease creating more bit errors. The noise floor limiting the SNR was that of the oscilloscope, with 3mV peak-to-peak on average.

Like the power assessment, 1244 realizations of 5Gbit/s data were captured to measure the BER in various turbulence strengths with the control on or off. 4 μ s of data was captured for each realization, and there was approximately 10ms between realizations. This longer delay was introduced in the control algorithm so that the high-speed camera (Phantom T-1340) could record the scanning and decision process, and make sure that each scan and decision point had at least one image. Each of the same turbulence strengths were tested, and the results are summarized in Figure 4.3:

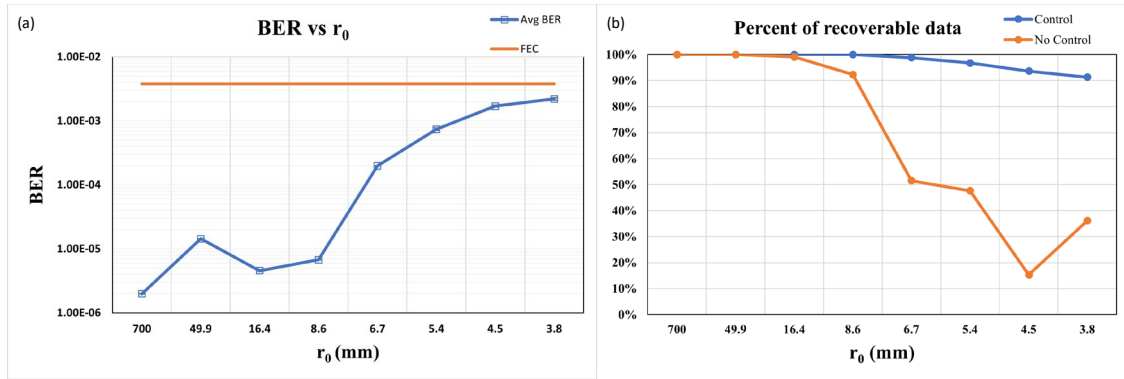


Figure 4.3. (a) mean BER for turbulence strength, control on. (b) percent BER below FEC limit

Figure 4.3 (a) shows the average BER for the communication link with the control system enabled, at various strengths of turbulence. As the turbulence increases, the system performance diminishes due to the diminished ability to correct for further beam wander. The threshold for determining what BER is acceptable for the given modulation scheme is the forward-error-correction limit (FEC limit), which for the PAM2 modulation is 3.8×10^{-3} . As indicated by the horizontal orange line, the average BER even in the strongest turbulence is still just below the recoverable limit. To assess the performance improvement of the control system vs. a stationary beam, Figure 4.3 (b) plots the percentage of the 1244 realizations that were recoverable below the FEC limit. With the control system on, even in the strongest turbulence, 90% of the realizations were recoverable. By contrast, the stationary beam's recoverability rapidly declines in stronger turbulence conditions.

It is important to consider again that the recoverability at $r_0 = 3.8$ mm could be improved with an increased OAM range. Figure 4.4 below shows a realization that was not recoverable, but two discrete signal levels can still be seen in the eye diagram:

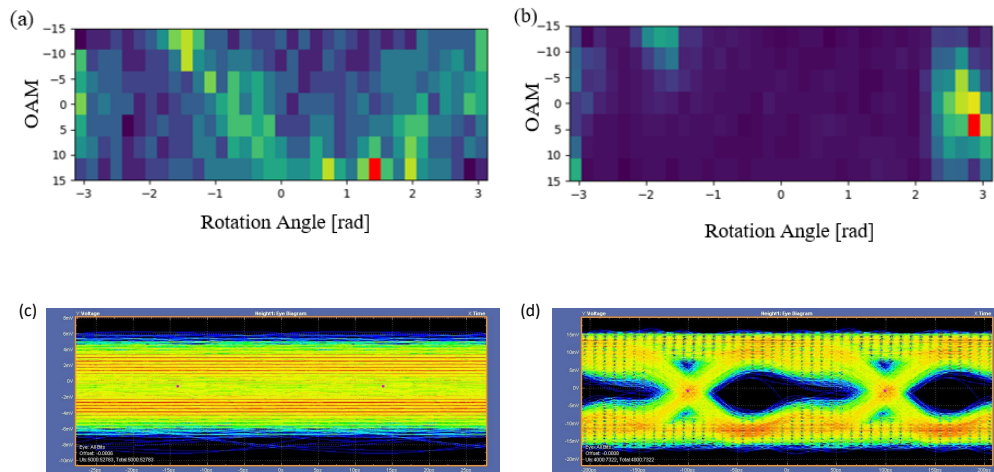


Figure 4.4. (a,c) realization above FEC limit. (b,d) realization below FEC

Notice that the chosen OAM for realization (a) was 15, corresponding to the maximal beam tilt. Most likely, this realization could have been recoverable if the system could compensate the tilt angle even further. By contrast, many of the realizations when the control system was off were completely lost and indistinguishable on the oscilloscope from noise. Figure 4.5 shows an example:

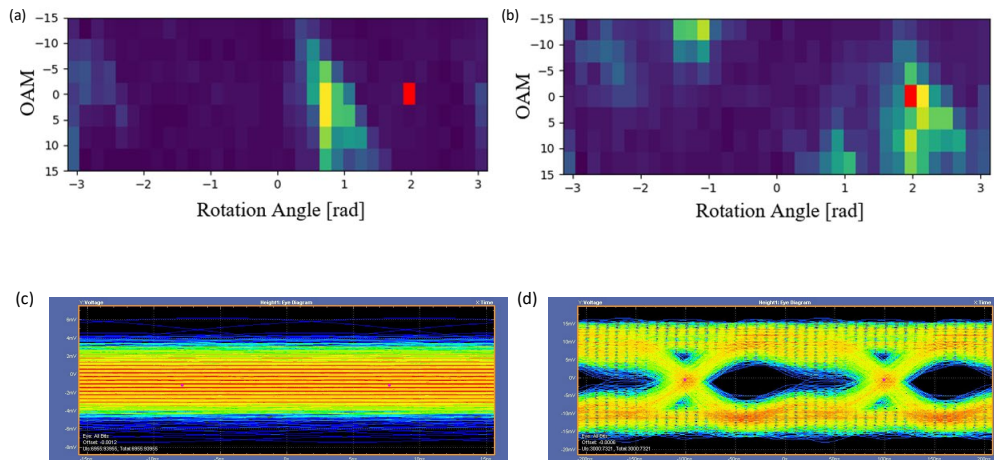


Figure 4.5. (a,c) beam deflected off axis. (b,d) beam guided to receiver

In (a), the results of the probing indicate that there was a good transmission path to the receiver within the probing space, but the stationary beam was not guided by this path.

Practically all the energy in the beam missed the detector, and the bit error rate would be much higher than the FEC limit. For the percentage of realizations without control that were recoverable, a probing result like (b) is expected. The stationary beam happens to be guided to the detector with a flat phase, and so the data is recoverable. Overall, this experiment shows that the control system significantly improves the resilience of a communication link in strong turbulence.

Multiple Channels and Higher Data Rate

The system as presented in this thesis can only manipulate a single Gaussian beam at a time. However, it is apparent from the probing results that several good transmission paths can exist in turbulence simultaneously. That is, different spatial locations about the vortex at different OAM states can simultaneously guide to the desired receiver. Using the HOBBIT architecture, multiple beams could be generated simultaneously using multiple frequencies on the AODs. To do this, a more advanced controller would be needed that could generate the waveforms itself, rather than controlling the waveform generator discussed in Chapter 3. Figure 4.6 shows an example of multiple channels existing at once:

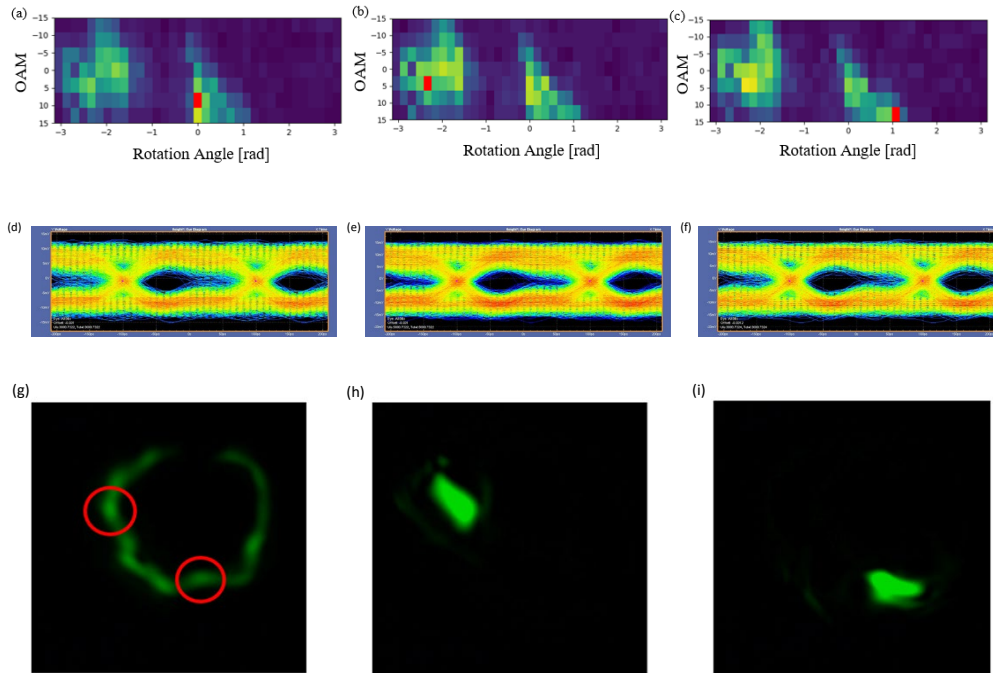


Figure 4.6. (a-f) Consecutive realizations. (g) Transmission channels, circled. (h,i) locked beams

In (a-c), the probing and decision point are shown for three consecutive realizations in the strongest turbulence. Notice the two distinct yellow channels, both of which indicate good power coupling to the detector. In (d-f), the corresponding eye diagrams show that the data is of good quality and easily recoverable, well below the FEC limit. Lastly, (g-i) show captured images from the high-speed camera for each of these realizations and the scan that shows the two transmission channels. To express the scalability of this concept, Figure 4.7 is shown:

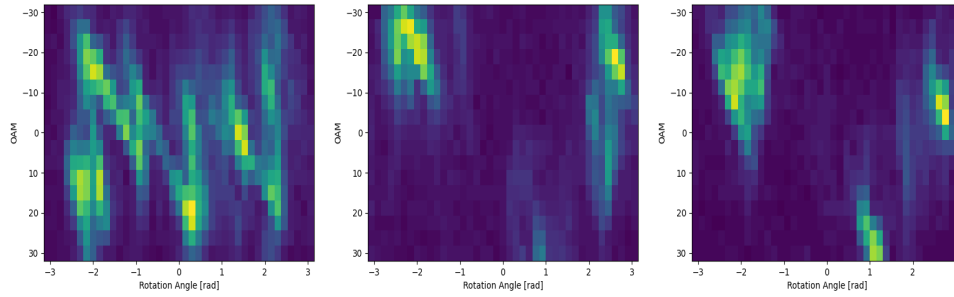


Figure 4.7. Multiple channels with higher OAM range

This figure shows some noteworthy probing results from an increased OAM range. Recall that, if the control system is disabled, the probing sequence can be manually expanded to a higher OAM range, and the results of the probing can still be recorded even though no beam will be locked into any of the channels. With an OAM range from -30 to 30, more channels can be seen at strong turbulence ($r_0 = 3.8\text{mm}$). If the controller could dynamically create the necessary waveforms to generate two or more Gaussian beams through the identified bright spots, there is potential to multiplex data or increase the total power delivered to a single location.

Another domain to expand the system's capability was the data rate applied to the beam. Though the oscilloscope was limited by its acquisition rate and memory to saving long realizations of 5Gbit/s data, the modulation system used on the beam could generate a 25Gbit/s signal using a 32 Quadrature Amplitude Modulation (QAM) scheme. This signal is described further in Appendix C. Using this modulation, the signal could be qualitatively measured over time by using the SignalVu software included with the oscilloscope. This software allows visualization of the recovered QAM constellations, which show the error-vector-magnitude (EVM) which can be translated to BER. Since

these realizations could only update several seconds apart, and could not be synchronized with probing data, a qualitative assessment was performed by watching the constellations and making general observations about the control system on vs. off. With the control system on, about 90% of the realizations seemed to be recoverable, while only about 30% were recoverable with the control off. Figure 4.8 below shows an example constellation received when the control system was on:

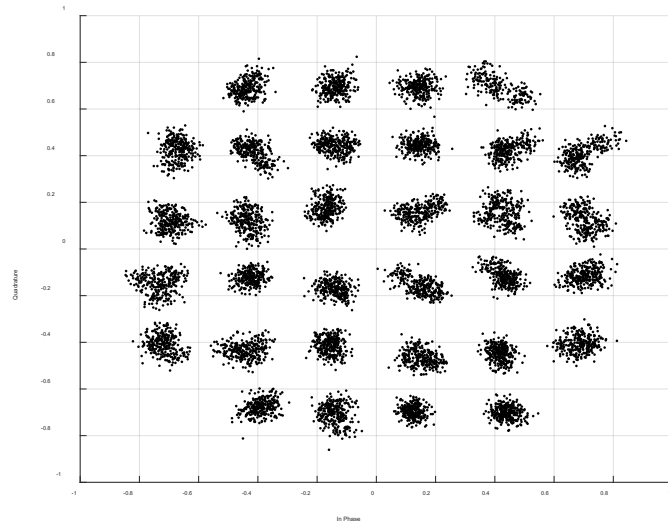


Figure 4.8. 32 QAM constellation

The constellation shown has a measured SNR of 20.7dB, which corresponds to a BER of 2.35×10^{-4} . The FEC limit for 32 QAM is 18.2dB. Most realizations with the control system on had a similar looking constellation, which would occasionally blur whenever the SNR dropped significantly. This test shows the capability of the system to support higher data rates even in strong turbulence, provided the receiving hardware can support this rate.

CHAPTER FIVE

CONCLUSIONS AND FUTURE WORK

The mitigation technique presented in the work has shown great success at transmitting power and a high-speed data link through atmospheric turbulence. Thanks to the rapid mode-switching capabilities of the HOBBIT system, a portion of the turbulent medium can be assessed and a transfer function for various input beam conditions can be used as feedback to a controller. While adaptive mitigation systems that work by expanding an effective aperture on the receiving side of an optical link are effective, using a corrective transmitter can leverage the focusing effect of waveguiding channels within turbulence. Additionally, from an engineering perspective, there are systems where corrective hardware would be more practical to implement on the transmission side.

Unlike conventional tip-and-tilt mirror controls, the HOBBIT system is entirely electronic, so there is no dependence on mechanical reliability. The HOBBIT architecture could support the exploitation of multiple transmission channels simultaneously using several Gaussian beams from the same output, in different spatial locations with different phases. With an enhanced control system, this could be straightforward to implement. The switching speed of the HOBBIT allows for a very fast probing of turbulence, currently $151\mu\text{s}$. Combined with the $750\mu\text{s}$ runtime on average of the control algorithm, the overall system refresh rate can keep up with the dynamics of even the most turbulent environment that could be generated in the laboratory.

The presented system is effective at mitigating the effects of turbulence on a single Gaussian beam, but there is great potential to improve the system that should be

investigated. The first improvement should be the development of a new control board that can apply electronic waveforms directly to the AODs of the HOBBIT system. This would involve a processor that interfaces with a high-speed digital-to-analog converter, and an analog-to-digital converter that could sample the feedback signal sufficiently fast. To control multiple beams simultaneously using the modified HOBBIT system, many different combinations of frequencies would be needed to feed the AODs. While the current waveform generator is limited in this capacity, a custom control board could store many combinations in memory or generate waveforms on the fly.

The next improvement could be made to the HOBBIT system itself, to expand the probing space to include the radial dimension as well as azimuthal. This would allow a greater region of air to be probed, likely finding more transmission channels in the volume. To do this, a third AOD could be added to the system to control this third dimension of the beam.

Another region of interest for the system is a way to integrate the feedback mechanism with the transmitter. Presently, the electrical feedback from the detector is wired to the transmitter. However, it is often desirable to contain a system to one physical location as much as possible. If optical scattering could be used as feedback, depending on the material used [31], the system could be self-contained and have applications in remote sensing and LIDAR. If a detector is used on the receiving system for the beam, perhaps another wireless protocol could be used to send feedback information to the controller. Lastly, the system should be tested in an underwater environment to assess its performance through turbulent water.

In conclusion, the controlled HOBBIT system is a unique and effective method for bypassing the undesirable distortions to an optical beam in atmospheric turbulence. It can maintain a beam's propagation path to a fixed receiving aperture with a flat phase, which allows for stability of a high-speed data link. The future of the system, with the described enhancements, is encouraging and could have great commercial applicability.

APPENDICES

Appendix A

Control Algorithm Code

```
# -----  
# Library Imports  
# -----  
  
# tested in python 3.9.5  
from scopefun import *  
from os import path  
import numpy as np  
import matplotlib.pyplot as plt  
from matplotlib.pyplot import axes  
import pandas as pd  
import math  
import time  
import imageio  
from pathlib import Path  
  
# -----  
# User Input  
# -----  
  
ctrlActive = 1 # 1 -> control is on. 0 -> control is off.  
numRealizations = 1 # How many cycles of scan -> hold do you want to run  
saveData = 0 # 1 -> raw data on .csv files will be saved. Use ImageProcess.py to make scalograms  
  
saveImages = 0  
  
bestAlign = 130 # which state you want to hold the beam to, if control is off. (numOAM*bestOAM + numPos*bestPos,  
# you will need to analyze a scalogram at 0% for this.)  
  
nOAM = 7 # number of OAM charge numbers  
nPos = 35 # number of theta steps  
interval = 615e-9 #time for each position during scan [s]  
fs = 5e6 # [samples/second]  
ds = 1/fs  
Options = nOAM*nPos  
  
scanDelayTime = 150000 # determines time of data TX/RX per scan. 150k -> ~3ms, 2.5M -> ~50ms. Experiment as  
desired
```

```

# -----
# Initialization
# -----

nSamples = int(4*np.ceil(fs*interval*nPos*nOAM/4)) #ensure divisibility by 4
T1 = interval/2
NBlock = np.round(T1/ds,decimals=0)
Duration = 2*T1*nPos*nOAM
nFrames = 1

BigMatrix = np.zeros([nSamples,Options]) DataCenters = np.arange
(start=T1, stop=Duration, step=2*T1) NDataCent = np.round
(DataCenters/ds,decimals=0) # find the central index of each
position

# configure Matrix for data processing of each scan. This matrix will effectively average the central points

# of each position scan
for x in range(Options):
    Row = np.zeros(nSamples)
    if fs == 12.5e6:
        length = Row[NDataCent[x].astype(int)-(NBlock/4).astype(int):NDataCent[x].astype(int)+
(NBlock/4).astype(int)].size
        Row[NDataCent[x].astype(int)-(NBlock/4).astype(int):NDataCent[x].astype(int)+(NBlock/4).astype(int)] =
np.ones(length)
    else:
        length = Row[NDataCent[x].astype(int)-1:NDataCent[x].astype(int)+2].size
        Row[NDataCent[x].astype(int)-1:NDataCent[x].astype(int)+2] = np.ones(length)
    BigMatrix[:,x] = Row.transpose()

if nSamples % 4 != 0:
    print("Err0: Number of samples must be divisible by 4")
    quit()

# calculate how much data is required for selected number of Samples
szHeader = 1024
szUsbPacket = 1024
szData = szHeader * (-(-nSamples//szUsbPacket)) # round up
szframe = szHeader + szData

fpga_image_file = path.relpath("fpga2.bin")

```

```

# -----
# init API
# -----

sfApiInit()          #USB conext
sfctx = sfCreateSFContext()  #SFContext
sfApiCreateContext(sfctx, 3072) #API buffer alloc

# -----
# activate API
# -----

if sflsActive(sfctx) == 0:
    sfSetActive(sfctx, 1)
    if sflsActive(sfctx) == 1:
        print("ScopeFun API activated")
else:
    print("ScopeFun API is active")

# -----
# open USB connection
# -----

susb = sfCreateSUsb()
susb.idVendor = 7504
susb.idProduct = 24836
print("Checking USB connection...", end = " ")
ret = sfHardwareOpen(sfctx, susb, 2)
if ret == 0:
    print("connected")
    # read FX3 firmware ID
    SEeprom = sfCreateSEeprom()
    ret = sfHardwareEepromReadFirmwareID(sfctx, SEeprom, 0)
    if ret == 0:
        np_eeprom_ID_bytes = np.array(SEeprom.data.bytes[0:14], copy=False)
        print("FX3 firmware ID:", np_eeprom_ID_bytes.tobytes())
    else:
        print("Reading FX3 firmware ID failed!")
else:
    print("not connected")
    print("Err0: Could not open USB connection!")
    quit()

```

```

# -----
# configure FPGA
# -----

print("Checking FPGA status...", end = " ")
# allocate SInt variable to hold FPGA status
status = sfCreateSInt()
ret = sfHardwareReadFpgaStatus(sfctx, status)
if status.value == 0:
    print("not configured")
    # create SFpga struct to hold FPGA image data and image size
    SFpga = sfCreateSFpga()
    # load FPGA image from file to numpy array
    fpga_image = np.fromfile(fpga_image_file, dtype=np.uint8)
    # set FPGA image size
    SFpga.size = fpga_image.size
    print ("Uploading FPGA firmware image (image file '{}', {} Bytes)"
           .format(fpga_image_file, fpga_image.size))
    # numpy array sizes must be the same before copy operation
    append_len = SFpga.data.bytes.size - fpga_image.shape[0]
    fpga_image = np.append(fpga_image, np.zeros(append_len, dtype=np.uint8))
    np.copyto(SFpga.data.bytes, fpga_image) # "SFpga.data.bytes" now holds FPGA image data

    del(fpga_image)
    sfHardwareUploadFpga(sfctx, SFpga) # upload FPGA firmware image
    time.sleep(1)
    ret = sfHardwareReadFpgaStatus(sfctx, status)
    if status.value == 0:
        print("Err0: FPGA configuration failed")
        quit()
    else:
        print("FPGA configuration successful")
else:
    print("configured")

```

```

# -----
# Configure hardware
# -----

print("Configuring hardware control registers...", end = " ")
SHw = sfCreateSHardware()
sfSetDefault(SHw) # set default settings

# Configure Digital Pins -> Note, digital pins are inverted by MOSFETs into the pattern jump on AWG

sfSetDigitalVoltage(SHw, 3.305, 0)
sfSetDigitalInputOutput(SHw,0,0) #configure all digital bits as outputs
for b in range(8):
    sfSetDigitalOutputBit(SHw,b,1) #initialize to scanning sequence
sfSetDigitalOutputBit(SHw,8,0) # scope trigger bit
sfSetDigitalOutputBit(SHw,9,0) #for measuring runtime

sfSetNumSamples(SHw, nSamples)
sfSetTriggerSource(SHw,1) #Use Channel 2 as trigger for Channel 1
sfSetTriggerSlope(SHw,1) #Falling Edge for trigger
sfSetXRange(SHw,6) # set X range (5: 80ns -> 12.5MHz) (6: 200ns -> 5MHz)
sfSetTriggerMode(SHw,2) # single acquisition
sfSetTriggerLevel(SHw,10) # level %

nReceived = sfCreateSInt()
nFrameSize = sfCreateSInt()
SFFHeader = SFrameHeader() # to hold frame header
SHwReceved = sfCreateSHardware() # to hold control regiters from received header

k=0
shift=2 # DO NOT CHANGE. This is position calibration for current timing setup. If setup changes, this should too

DataList = []
DecisionList = []

```



```

while k<numRealizations:
    # -----
    # Scanning Section
    # -----

    sfSetTriggerReArm(SHw,1) # re arm bit
    #sfSetDigitalOutputBit(SHw,9,1) #for measuring runtime
    sfHardwareConfig(sfctx,SHw)
    ret = sfFrameCapture(sfctx, nReceived, nFrameSize)
    sfSetTriggerReArm(SHw,0) # re arm bit
    sfHardwareConfig(sfctx,SHw)
    frameSizeBytes = nFrameSize.value      # frame size
    receivedBytes = nReceived.value        # received bytes after calling sfFrameCapture()

    totalReceivedBytes = sfctx.frame.received # total received bytes (will be zero if full frame was received)

    sfGetHeader(sfctx, sfctx.frame.data, SFFHeader) # copy frame header to SFFHeader struct

    sfGetHeaderHardware(SFFHeader, SHwReceivied) # read control registers from header
    nSamplesInFrame = sfGetNumSamples(SHwReceivied) # get number of _received_ samples from header

    # -----
    # Decision Section
    # -----

    frameData = np.array(sfctx.frame.data.data.bytes[szHeader:frameSizeBytes], copy=False) # read raw data from
    captured frame
    ch1 = sfGetSamplesFromBytes(1, nSamplesInFrame, frameData) # decode raw data

    # uncomment the next line if you want to get the data for the trigger to the control board (mostly useless):

    #ch2 = sfGetSamplesFromBytes(2, nSamplesInFrame, frameData)

    yAvg = np.dot(ch1,BigMatrix)
    midx = np.argmax(yAvg)
    Decision = midx+shift #correct position offset
    if Decision > 244:
        Decision = Decision - Options
    if ctrlActive == 0:
        Decision = bestAlign # best point for alignment

```

```

# -----
# Digital Output Section
# -----

# set bits to correct jump in sequence
for i in range(8):
    sfSetDigitalOutputBit(SHw,i,~Decision>>i&1)

# turn on trigger signal for Data Oscilloscope (comment if you don't want to trigger data)

sfSetDigitalOutputBit(SHw,8,1)
sfHardwareConfig(sfctx, SHw)

# store results for post processing
if saveData:
    DataList.append(yAvg)
    DecisionList.append(Decision)

# delay program for data transmission
for d in range(scanDelayTime):
    pass

# reset scanning sequence and data trigger (comment if you want to hold beam at decision, but that will only
# work if you are running one realization or program will
get stuck)
for i in range(8):
    sfSetDigitalOutputBit(SHw,i,1)

sfSetDigitalOutputBit(SHw,8,0)
#sfSetDigitalOutputBit(SHw,9,0) #for measuring runtime
sfHardwareConfig(sfctx, SHw)
#for d in range(scanDelayTime): #if you want to delay scans to see on high speed camera

# pass
k=k+1 #loop iteration

print("Finished!")
#Decision = 250 # Turn off laser when full process is complete
#for i in range(8):
# sfSetDigitalOutputBit(SHw,i,~Decision>>i&1)
#sfHardwareConfig(sfctx, SHw)

```

```

OAMChoices = []
AngleChoices = []

# -----
# Save Scanning Data
# -----

if saveData == 1:
    for i in range(k):
        OBi = np.int64((DecisionList[i]/nPos)//1)
        TBi = DecisionList[i] % nPos
        OAMChoices.append(OBi)
        AngleChoices.append(TBi)

    OAMChoiceArr = np.array(OAMChoices)
    AngleChoiceArr = np.array(AngleChoices)
    DataArr = np.array(DataList)

    if saveImages == 1:
        imageData = np.reshape(DataList[i],(nOAM,nPos))
        imageData = np.roll(imageData,shift)
        cmap = plt.cm.viridis
        norm = plt.Normalize(imageData.min(),imageData.max())
        rgba = cmap(norm(imageData))
        if ctrlActive==1:
            rgba[OBi.astype(int),TBi.astype(int), :3] = 1,0,0
        else:
            rgba[OBi,TBi, :3] = 1,0,0
        tit = "Frame " + str(i+1)
        plt.title(tit)
        plt.xlabel("Theta [rad]")
        plt.ylabel("OAM")

        plt.imshow(rgba,extent=[-1*math.pi, math.pi, 15, -15],aspect = (1*math.pi)/41)#,cmap="hot")

        tit2 = "image" +str(i) + ".png"
        plt.savefig(tit2)

# CHANGE FILE PATH TO WHATEVER DIRECTORY YOU WANT, KEEP .csv FILE NAMES THE SAME
pd.DataFrame(OAMChoiceArr).to_csv("C:/Users/martynl/Desktop/HOBBIT Comm System (Palantir)/OAMs.csv")

pd.DataFrame(AngleChoiceArr).to_csv("C:/Users/martynl/Desktop/HOBBIT Comm System (Palantir)/Thetas.csv")

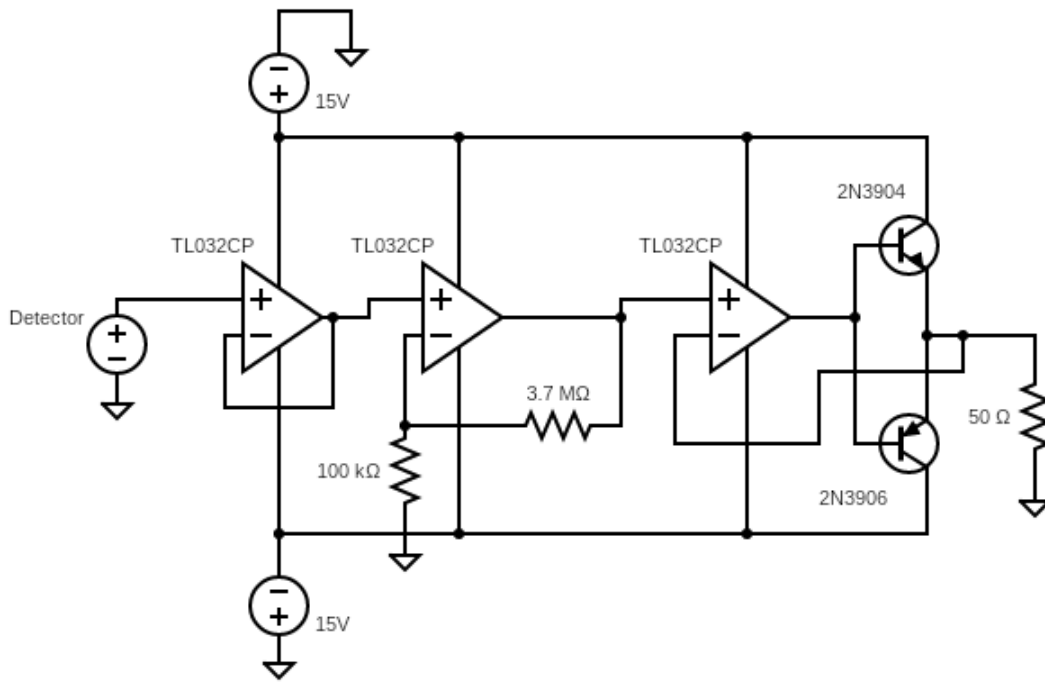
pd.DataFrame(DataArr).to_csv("C:/Users/martynl/Desktop/HOBBIT Comm System (Palantir)/Data.csv")

```

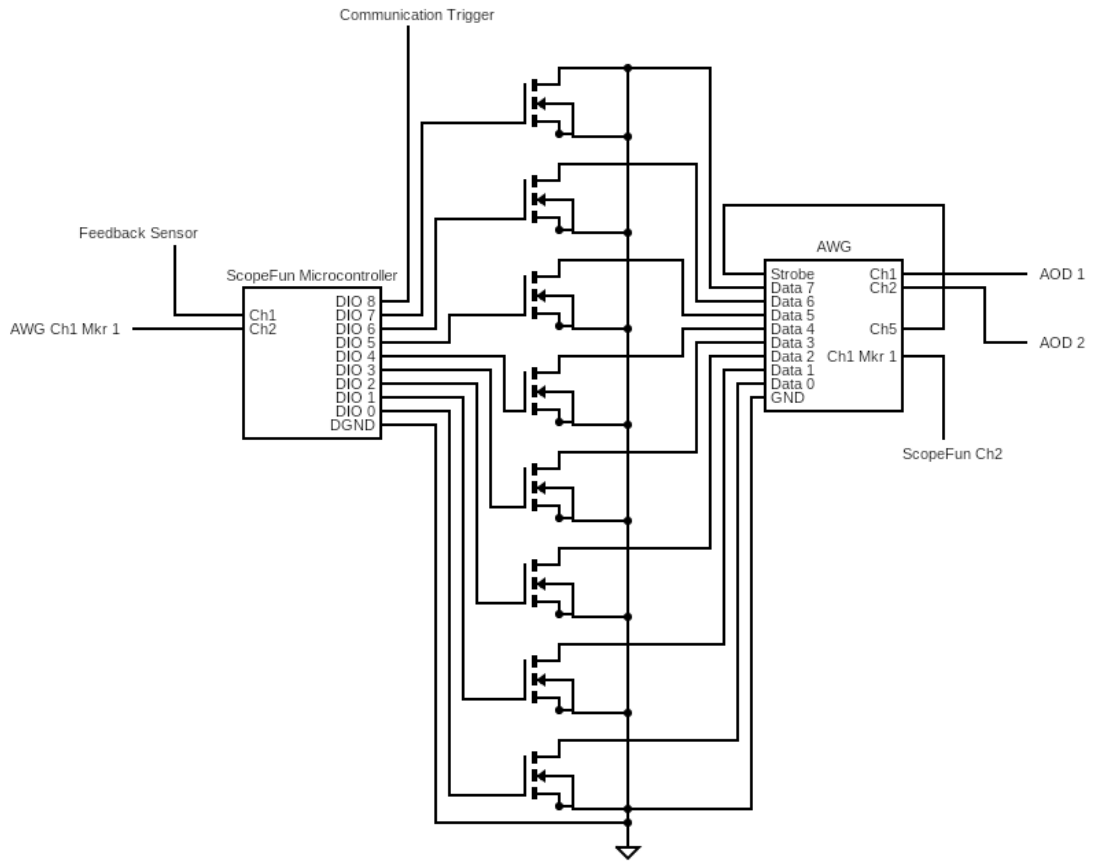
Appendix B

Circuit Diagrams

Amplifier Circuit for Power Measurement



Circuit Diagram of Control Hardware



Appendix C

Description of Data Signals

The signal applied to the phase modulator is represented by equation (1). The signal amplitude, a_k , determines the voltage level into the phase modulator taking on ± 500 mV. A symbol rate of 5 GHz gives a symbol period, T_s , of 0.2 ns. For the PAM2 signal, each symbol only consists of a single bit which gives an overall data rate of 5 Gbit/s for the channel.

$$s_{PAM2}(t) = \sum_{n=-\infty}^{\infty} a_k \text{rect}(t - nT_s) \quad (1)$$

Another signal used to qualitatively test the system was a 32 QAM (quadrature amplitude modulated) signal. This signal is defined by equation (2). The signal amplitude, a_k , and the phase term, φ_k , can take on 6 unique values. For the 32 QAM signal, f_c is the carrier frequency. The symbol period is unchanged, but each symbol represents a 5-bit combination achieving a data rate of 25 Gbit/s per channel.

$$s_{32QAM}(t) = \sum_{n=-\infty}^{\infty} a_k \cos(2\pi f_c t + \varphi_k) \text{rect}(t - nT_s) \quad (2)$$

To determine the quality of the data transmitted through the channels, the BER of the signal must be calculated. The BER calculations for each of the signals can be seen in equations (3-6). The average voltages of the two levels are μ_1 and μ_0 . The standard deviation for each level is σ_1 and σ_0 . The threshold voltage which determines the separation between levels is V_{th} . $\text{erfc}()$ is the complementary error function. In (the QAM BER) equation (5), M represents the number of points in the constellation. The error vector magnitude (EVM) is the error between each measured constellation point and

the theoretical constellation point. The relationship between EVM and signal-to-noise ratio (SNR) is shown in equation (6) [32].

$$BER_{PAM2} = \frac{1}{4} \operatorname{erfc} \left(\frac{\mu_1 - V_{th}}{\sigma_1 \sqrt{2}} \right) + \frac{1}{4} \operatorname{erfc} \left(\frac{V_{th} - \mu_0}{\sigma_0 \sqrt{2}} \right) \quad (3)$$

$$V_{th} = \frac{\mu_0 \sigma_1 + \mu_1 \sigma_0}{\sigma_0 + \sigma_1} \quad (4)$$

$$BER_{32QAM} = \frac{1 - M^{-\frac{1}{2}}}{\frac{1}{2} \log_2 M} \operatorname{erfc} \left(\sqrt{\frac{3/2}{(M-1)EVM_{rms}^2}} \right) \quad (5)$$

$$SNR \approx \frac{1}{EVM_{rms}^2} \quad (6)$$

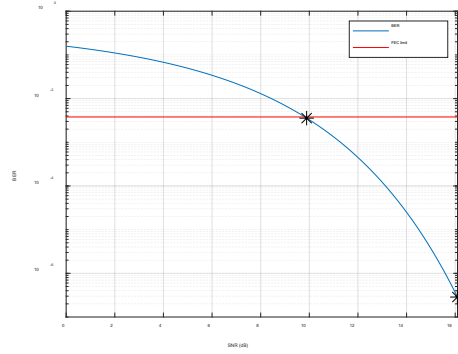


Fig. 1. Bit error rate vs. Signal to noise ratio. Right marker: System SNR with 6mW of input power to HOBBIT system at ambient turbulence. Left marker: ~6dB below reference power, just below the FEC limit

Appendix D

Optical Transform of HOBBIT System

The $532nm$ laser source into the modified HOBBIT system had a beam diameter of $1.1mm$ after the fiber collimator (F110APC-532). This beam was imaged onto the center of the first AOD by a 5x reducing telescope (GBE05-A). The first AOD controlled the tilt angle of the first diffracted order of the AOD; the Fourier transform of this tilt angle resulted in the spatial shift of the Gaussian beam on the first log-polar optic. This tilt angle was controlled by applying an RF signal to the AOD. The first-order diffracted beam from the first AOD can be described by

$$E_1(x, y) = \exp\left(-\frac{x^2 + y^2}{w_1^2} - j(k_x x + k_z z + 2\pi(f_c + f_{A1})t)\right) \quad (1)$$

where $w_1 = 0.11mm$ is the diameter of the Gaussian beam intensity (radius of the field), k_x and k_z are the x and z components of the k vector, f_c is the center frequency of the laser, and $f_{A1} = f_{01} + \Delta f_1$ is the frequency applied to the AOD, with $f_{01} = 95MHz$ the center frequency of the first AOD. The k vector is related to the frequency applied to the AOD by $k_x = 2\pi / \lambda \sin(\lambda \Delta f_1 / V) \approx 2\pi \Delta f_1 / V$ and $k_z = 2\pi / \lambda \cos(\lambda \Delta f_1 / V)$, where $\lambda = 532nm$ is the wavelength and $V = 650m/s$ is the acoustic velocity of the AOD. The lens focal length was $150mm$ and the lens was placed a focal length away from the first AOD and a focal length away from the first log-polar optic. This resulted in the Fourier transform of the beam in the first AOD onto the first log-polar optic. The Fourier transform of Eq. (1) is given by

$$\hat{E}_1(x, y) = \frac{1}{\pi w^2} \exp\left(-\frac{(x-x_0)^2 + y^2}{\sigma^2} - j(2\pi(f_c + f_{A1})t)\right) \quad (2)$$

where $\sigma = \lambda F / (\pi w_1) = 0.23mm$, $F = 150mm$ is the focal length of the lens, and $x_0 = \Delta f_1 \lambda F / V$ is the spatial shift on the first log-polar optic. This spatial shift is mapped to rotation by the log-polar optics. Due to the design parameters of the log-polar optics, a spatial shift of $\pm 3mm$ rotated the beam $\pm \pi$ radians. The bandwidth required for a full rotation is $49MHz$. A half-wave plate was located between the two AODs; the AODs are shear mode and rotate the polarization of the first order diffracted beam. The half-wave plate was used to rotate the polarization of the first order diffracted beam from the first AOD back to the proper input polarization that is required by the second AOD. The second AOD was responsible for the OAM on the probe beam; it tilts the laterally displaced gaussian beam before the log-polar optics. This tilt was then mapped to OAM. The second AOD was placed as close as possible to the first log-polar optic to minimize the effect of lateral displacement from propagation. The distance from the center of the second AOD to the first log-polar optic was $40mm$. The field incident on the first log-polar optic can be expressed as

$$E_{in} = \exp\left(-\frac{(x-x_0)^2 + (y-y_0)^2}{\sigma^2} - j\left(\frac{2\pi\Delta f_2}{V}x + 2\pi(f_c + f_{A1} + f_{A2})t\right)\right) \quad (3)$$

where $y_0 = -0.147mm$ denotes the relative height of the beam to the center of the log-polar optics, $f_{A2} = f_{02} + \Delta f_2$ is the frequency applied to the second AOD, and $f_{02} = 120MHz$ the center frequency of the second AOD. This field in Eq. (3) was then mapped by the log-polar optics. The log-polar coordinate transform is given by

$$\begin{aligned} u &= A\theta \\ v &= -A \ln\left(\frac{r}{B}\right) \end{aligned} \quad (4)$$

where $(x=u, y=v)$ are coordinates in the plane of the first log-polar optic and (r, θ) are polar coordinates in the plane of the second log-polar optic [1]. The constants A and B are design parameters of the transform, where we have $A = 0.955\text{mm}$ and $B = 1.5\text{mm}$. The log polar transform is then applied and seen in Eqn. (1) in the main text to create the main field of the HOBBIT system output.

APPENDIX E

LIST OF PUBLICATIONS

1. M. Lemon, E. Robertson, J. Free, K. Dai, J. K. Miller, L. Vanderschaaf, M. Cox, R. Watkins, and E. G. Johnson., “Sensing and coupling of optical channels in dynamic atmospheric turbulence using OAM beamlets for improved power and data transmission,” Manuscript in preparation 2022.
2. M. Lemon, E. Robertson, J. Free, K. Dai, J. K. Miller, M. Cox, L. Vanderschaaf, R. Watkins, and E. G. Johnson., “HOBBIT Probing of Turbulence and Channel Excitation in Real-Time for Free-Space Communications,” Frontiers in Optics and Laser Science 2022, Rochester, NY, USA, 9 October 2022

REFERENCES

1. V. Tatarskii, "Wave Propagation in a Turbulent Medium," McGraw-Hill, New York, 1961
2. M. Vorontsov, V. Kolosov, A. Kohnle., "Adaptive laser beam projection on an extended target: phase- and field-conjugate precompensation," in *Journal of the Optical Society of America*, vol. 24, no. 7, pp. 1975-1993, 22 December 2006
3. P. Lushnikov, N. Vladimirova., "Toward Defeating Diffraction and Randomness for Laser Beam Propagation in Turbulent Atmosphere," in *Jetp Lett*, vol. 108, no. 9, pp. 571–576, 24 September 2018
4. C. Friehe *et al.*, "Effects of temperature and humidity fluctuations on the optical refractive index in the marine boundary layer," in *Journal of the Optical Society of America*, vol. 65, no. 12, December 1975
5. M. Beason, S. Gladysz, L. Andrews., "Comparison of probability density functions for aperture-averaged irradiance fluctuations of a Gaussian beam with beam wander," in *Applied Optics*, 59, 6102-6112, 10 July 2020
6. H. Kaushal *et al.*, "Experimental Study on Beam Wander Under Varying Atmospheric Turbulence Conditions," in *IEEE Photonics Technology Letters*, 23, 1691-1693, 15 November 2011
7. L. Andrews *et al.*, "Strehl ratio and scintillation theory for uplink Gaussian-beam waves: beam wander effects," in *Optical Engineering*, 45, no. 7, July 2006
8. N. Védrenne, M. Toyoshima, A. Guérin., "Turbulence effects on bi-directional ground-to-satellite laser communication systems," International Conference on

Space Optical Systems and Applications 2012, 10-1, Corsica, France, October 2012

9. D. Schlipf *et al.*, "Lidar-based Estimation of Turbulence Intensity for Controller Scheduling," 2020 Journal of Physics: Conference Series, 1618, September 2020
10. J. Jabczyński, P. Gontar., "Impact of atmospheric turbulence on coherent beam combining for laser weapon systems," in Defense Technology, 17, pp. 1160-1167, 2021
11. A. Klug, C. Peters, A. Forbes., "Robust structured light in atmospheric turbulence". 2022
12. R. Kumar *et al.*, "Air Turbulence Mitigation Techniques for Long-Range Terrestrial Surveillance," in *IETE Technical Review*, vol. 34, no. 4, pp. 416-430, August 2016
13. H. Zhou *et al.*, "Demonstration of Turbulence Resiliency in a Mode-, Polarization-, and Wavelength-Multiplexed Free-Space Optical Link Using Pilot-Assisted Optoelectronic Beam Mixing," in *Journal of Lightwave Technology*, vol. 40, no. 3, pp. 588-596, 1 February 2022
14. X. Zhu, J. Khan., "Free-Space Optical Communication Through Atmospheric Turbulence Channels," in *IEEE Transactions on Communications*, vol. 50, no. 8, pp. 1293-1300, August 2002
15. A. Puryear, V. Chan, "Optical communication through the turbulent atmosphere with transmitter and receiver diversity, wavefront control, and coherent

- detection”, SPIE Optical Engineering + Applications 2009, San Diego, CA, USA, 21 August 2009
16. B. Ellerbroek, T. Rhoadarmer., “Adaptive Wavefront Control Algorithms for Closed Loop Adaptive Optics,” in *Mathematical and Computer Modeling*, vol 33, pp. 145-158, June 2001
 17. A. Kudryashov *et al.*, “Real-time 1.5kHz adaptive optical system to correct for atmospheric turbulence,” in *Optics Express*, vol. 28, no. 25, 7 December 2020
 18. Y. Wang *et al.*, “Performance analysis of an adaptive optics system for free space optics communication through atmospheric turbulence,” in *Scientific Reports*, vol. 8, no. 1124, 18 January 2018
 19. N. Védrenne *et al.*, “Adaptive Optics for high data rate satellite to ground laser link,” SPIE LASE, 2016, San Francisco, California, United States, February 2016
 20. M. Zhao *et al.*, “Aberration corrections for free-space optical communications in atmosphere turbulence using orbital angular momentum states,” in *Optics Express*, vol. 20, no. 1, 2 January 2012
 21. M. Cox *et. al.*, “Structured Light in Turbulence,” in *IEEE Journal of Selected Topics in Quantum Electronics*, vol. 27, no. 2, March 2021
 22. A. van Eekeren *et al.*, “Turbulence Compensation: an overview,” SPIE 8355 Infrared Imaging Systems: Design, Analysis, Modeling and Testing XXIII, May 2012

23. W. Li *et al.*, “Rapidly tunable orbital angular momentum (OAM) system for higher order Bessel beams integrated in time (HOBBIT),” in *Optics Express*, vol. 27, no. 4, 18 February 2019
24. L. Allen *et al.*, “Orbital angular momentum of light and the transformation of Laguerre-Gaussian laser modes,” in *Physical Review A*, vol. 45, no. 11, 1 June 1992
25. S. Qiu *et al.*, “Directly observing the skew angle of a Poynting vector in an OAM carrying beam via angular diffraction,” in *Optics Letters*, 46, 3484-3487, 15 July 2021
26. E. Johnson *et al.*, “Higher-order Bessel beams integrated with time (HOBBIT) for dynamic structured light control,” in *SPIE* vol. 11297, 24 February 2020
27. J. Free *et al.*, “Rapidly Reconfigurable Pulsed Higher Order Bessel Beams,” in *Frontiers in Optics*, OSA 2020
28. K. Dai, J.K. Miller, E. Johnson, “Wavefront Sensing based on a 2D HOBBIT,” in *Frontiers in Optics*, Optica Publishing Group 2021
29. R. Watkins *et al.*, “Experimental probing of turbulence using a continuous spectrum of asymmetric OAM beams,” in *Optics Express*, vol. 28, no. 2, 20 January 2020
30. M. Cox *et al.*, “Experimental Results on the Effect of OAM State on the Scintillation Index for an Asymmetric Perfect Vortex Beam,” 2021 *Frontiers in Optics and Laser Science*, Rochester NY USA, 18 October 2022

31. M. Voronstov, V. Kolosov, "Adaptive focusing of laser radiation onto a rough reflecting surface through the turbulent and nonlinear atmosphere," 11th International Symposium on Atmospheric and Ocean Optics/Atmospheric Physics, Tomsk, Russian Federation, 2004
32. R. A. Shafik, M. S. Rahman and A. R. Islam, "On the Extended Relationships Among EVM, BER and SNR as Performance Metrics," 2006 International Conference on Electrical and Computer Engineering, pp. 408-41